BNL-226462-2025-JAAM

GRP-COSC-10

A highly oxygen reduction reaction active and CO2 durable high-entropy cathode for solid oxide fuel cells

F. He, K. Sasaki

To be published in "Applied Catalysis B: Environment and Energy"

October 2024

Chemistry Department

Brookhaven National Laboratory

U.S. Department of Energy

USDOE Office of Energy Efficiency and Renewable Energy (EERE), Office of Sustainable Transportation. Hydrogen Fuel Cell Technologies Office (HFTO)

DISCLAIMER

A Highly Oxygen Reduction Reaction Active and CO_2 Durable High-entropy Cathode for Solid Oxide Fuel Cells

Fan He[1], Feng Zhu[1], Kang Xu[1], Yangsen Xu[1], Dongliang Liu[2], Guangming Yang[2], Kotaro Sasaki[3], YongMan Choi[4]*, and Yu Chen[1]*

[1]School of Environment and Energy, South China University of Technology, 382 East Road, Higher Education Mega Center, Guangzhou 510006, P. R. China.

[2]State Key Laboratory of Materials-Oriented Chemical Engineering, College of Chemical Engineering, Nanjing Tech University, Nanjing 210009, P. R. China.

[3]Chemistry Division, Brookhaven National Laboratory, Upton, NY 11973, USA.

[4]College of Photonics, National Yang Ming Chiao Tung University, Tainan 71150, Taiwan

*Corresponding authors: YongMan Choi (ymchoi@nycu.edu.tw); Yu Chen (eschenyu@scut.edu.cn)

Abstract

One big obstacle for the oxygen reduction reaction (ORR) electrode in solid oxide fuel cells (SOFCs) is the poor reaction activity and fast degradations caused by CO_2 poisoning. Here we report our design of an active A-site Ca-rich high-entropy $Pr_{0.1875}Ba_{0.1875}Sr_{0.1875}La_{0.1875}Ca_{0.25}CoO_{3-\delta}$ (PBSLC$_{25}$C) electrode, guided by the O p-band theory. When applied as a cathode in solid oxide fuel cells (SOFCs), it demonstrates high ORR activity and excellent CO_2 tolerance under realistic operating conditions. Ni-YSZ-based anode-supported cells with PBSLC$_{25}$C cathodes demonstrate excellent peak power densities of 1.14 W cm^{-2}, 1.04 W cm^{-2}, and 0.77 W cm^{-2} in the air with 1%, 5%, and 10% CO_2, respectively, at 750 °C. The engineered high-entropy PBSLC$_{25}$C effectively diminishes the CO_2 poisoning effect and maintains active surfaces for fast oxygen exchange, as confirmed by the cell durability test in air containing CO_2 (5 and 10 vol%), Raman spectroscopy, and density functional theory calculations.

Keywords: Solid oxide fuel cells, cathode, high-entropy perovskite, oxygen reduction reaction, CO_2 tolerance.

1. Introduction

Solid oxide fuel cells (SOFCs) offer promising prospects for the most efficient energy utilization and conversion using flexible fuels.[1-3] Rapid attention has been focused on the rational design of cathodes, which could contribute the most to the degradation of cell performance during the operation.[4, 5] Oxygen reduction reaction (ORR) activity as an important parameter is of high merit in revealing the properties of functional cathodes.[6-8] However, the kinetics of ORR are complicated especially under realistic operating conditions with contaminations (e.g., CO_2, H_2O, or/and Cr), limited by one or more steps.[9, 10] The electrochemical performance and stability of SOFCs are highly restricted by a largely increasing polarization resistance (R_p) of cathode due to the dramatic poisoning from contaminations on the oxygen reduction reaction (ORR) activity.[11, 12] Thus, future market penetration of SOFC technique requires a further innovation of active and durable cathodes to prolong the cell/system lifetime.

A descriptor (e.g., O *p*-band center, bulk vacancy energy, and charge-transfer energy) can demonstrate the key energetics underlying the ORR activity of the cathodes for high-performance SOFCs.[13-15] Among which, O *p*-band center as a theoretical descriptor is effective, and can realize the reliable prediction of ORR activity without the details of the complex electrode surface.[13, 16] Adjusting the position of the O *p*-band center approaching the Fermi level can optimize the kinetics of the surface oxygen exchange and chemisorption energies. This method was extensively utilized for material designs of highly active catalysts in the field of electro-catalysis.[17, 18] Even under elevated temperatures, the perovskite oxides with the disordered structure can be computationally investigated by employing special quasirandom structures (SQS).[19] A descriptor of O *p*-band center is utilized effectively as a practical theoretical tool for the development of optimal cathode catalysts in SOFCs.

The screened electrodes on basic of oxygen *p*-band center can enhance the long-term durability and intrinsic tolerance against contaminants poisoning.[20, 21] According to the theoretical calculations of CO_2 adsorption energy, $PrBa_{0.8}Ca_{0.2}Co_2O_{5+\delta}$ (PBCC) perovskite materials have been currently investigated as a robust cathode for enhancing structural stability against CO_2 poisoning.[11] The PBCC electrode exhibited the excellent durability in air containing CO_2, comprehensively verified by the stabilities of typical symmetrical cells (~1000 h) and single cells (~400 h) in CO_2-containing atmospheres.[11] A-site Ca substitution is chosen as a reasonable optimization strategy for the contaminant-tolerance electrodes with the guidance of the density functional theory (DFT) calculations.[22] $SrCoO_{3-\delta}$-type perovskite materials have been extensively verified as high-performance cathodes for SOFCs due to their high O *p*-band values.[23-25] Theoretically, Sr^{2+} in the perovskite lattice can accelerate the intrinsic exchange kinetics of oxygen reduction and evolution reactions at the electrode surface.[26, 27] While the activity of such $SrCoO_{3-\delta}$-type electrodes is likely limited by the poor structural durability due to the severe surface Sr enrichment at elevated temperatures.[28] To maximize the role of Sr^{2+} cation in the $SrCoO_{3-\delta}$-type perovskite materials, it is vital to improve the electrode durability and even tolerance against contaminants. The non-redox element (e.g., Nb, Ta, and Zr) doping strategy has been reported as an exceptional optimization on the structural stability of the electrode for a long-term operation.[29] In addition, the concept of entropy stabilization has been extensively studied for the active and robust cathodes via effectively restraining the Sr^{2+} segregation.[12, 30, 31] The contribution of multivariant A-site cations (e.g., Sr, Ca, and Pr etc.) can perform the interesting synergistic effects in the system of the high-entropy perovskite oxides.[30, 32]

Inspired by those studies, herein we report a novel high-entropy perovskite oxide $Pr_{0.1875}Ba_{0.1875}Sr_{0.1875}La_{0.1875}Ca_{0.25}CoO_{3-\delta}$ ($PBSLC_{25}C$) with A-site Ca cation rich, displaying a boosted electrochemical performance and an excellent durability against CO_2 (up to 10%). The anode-supported cells with the $PBSLC_{25}C$ cathode achieved remarkable peak power densities of 1.14 W cm^{-2}, 1.04 W cm^{-2}, and 0.77 W cm^{-2} at 750 °C in the air with different concentrations (varies from 1%, 5%, and 10% CO_2) of CO_2, respectively. It was found that the main contribution to the increasing resistance during the CO_2 poisoning process could be the electrode reaction of the surface gas-related diffusion, as analyzed by the distribution of relaxation time (DRT). On the other hand, the polarization resistance of the $PrBa_{0.8}Sr_{0.2}CoO_{6-\delta}$ (PBSC) cathode increased dramatically from 0.021 (in air) to 0.186 Ω cm^2 (in air with 5% CO_2), due likely to the aggravated formation of $SrCO_3$ deposited on the electrode surface under the condition of a high CO_2 concentration. The durability of symmetrical cells (300 h) and single cells (100 h) in air containing 5% and 10% CO_2 strongly indicate that the high-entropy $PBSLC_{25}C$ cathode exhibits robust surface characteristics for an enhanced CO_2-tolerance, as probed by Raman spectroscopy and DFT calculations.

2. Experimental section

2.1. Materials synthesis

The high-entropy perovskite of $Pr_{0.1875}Ba_{0.1875}Sr_{0.1875}La_{0.1875}Ca_{0.25}CoO_{3-\delta}$ ($PBSLC_{25}C$) was synthesized by a sol-gel complexing method. Based on the nominal composition of $PBSLC_{25}C$, $Pr(NO_3)_3\cdot 6H_2O$, $Ba(NO_3)_2$, $Sr(NO_3)_2$, $Ca(NO_3)_2$, $La(NO_3)_3$, and $Co(NO_3)_2\cdot 6H_2O$ were stoichiometrically added into the deionized water with complexing agents of EDTA and citric acid. Ammonia solution was then added to adjust the pH of the solution. The solution was continuously stirred and heated at 90 °C to form a gel. Subsequently, the achieved gel was dried at 250 °C for 5 h in an oven. Finally, the precursors were pre-calcined at 950 °C for 2 h, and then sintered at 1000 °C for 5 h to obtain $PBSLC_{25}C$ powders. Some samples of

$PrBa_{0.8}Sr_{0.2}CoO_{6-\delta}$ (PBSC), $PrBa_{0.8}Ca_{0.2}CoO_{6-\delta}$ (PBCC), and $Pr_{0.2}Ba_{0.2}Sr_{0.2}La_{0.2}Ca_{0.2}CoO_{3-\delta}$ (PBSLCC) were prepared by the same method, and all ccalcined at 1000 °C for 5 h. The anode and electrolyte powders of NiO, $Zr_{0.84}Y_{0.16}O_{2-\delta}$ (YSZ), and $Gd_{0.1}Ce_{0.9}O_{2-\delta}$ (GDC) were purchased from H2-BANK. $La_{0.8}Sr_{0.2}Ga_{0.8}Mg_{0.2}O_{3-\delta}$ (LSGM) was synthesized by a solid-state reaction method. LaO, $SrCO_3$, MgO, and Ga_2O_3 as raw materials were mixed by ball milling for 12 h, and then calcined at 1250 °C for 5 h to obtain final powders.

2.2. Cell preparation

The LSGM powder was dry-pressed into green pellets and then sintered at 1450 °C for 5 h to obtain the dense pellets. Dense LSGM pellets with a thickness of 400 μm were prepared for symmetrical tests. The anode-supported half cells were fabricated by a co-tape casting method, which has been reported in our previous works.[33, 34] To eliminate the adverse reactions between the cathode and YSZ electrolyte, the GDC buffer layer was drop-coated onto the NiO-YSZ|YSZ half cells, and then co-sintered at 1300 °C for 2 h. The solution of the GDC buffer layer is composed of GDC powder, ethyl cellulose, terpinol, and acetone with a weight ratio of 1:0.15:1.85:10. The cathodes were then screen-printed on the GDC buffer layer and then sintered at 1000 °C for 2 h. The as-fabricated symmetrical cells were also sintered at 1000 °C for 2 h for further tests. The cathode ink for the screen-printing was composed of the cathode powder, ethyl cellulose, and terpinol with a weight ratio of 1:0.04:0.76. The effective area of single cells was 0.2826 cm^{-2}. The silver wires were used as current collectors.

2. 3. Characterization and electrochemical tests

X-ray diffraction (XRD) measurements were conducted by a Bruker D8 Advance diffractometer (Bruker, Germany) using Cu Kα radiation (λ=0.15406 nm). The microstructure and morphology of samples were observed by scanning electron microscopy (SEM) (Hitachi SU8010, Japan) and transmission electron microscopy (TEM) (TF20). The electrical conductivity relaxation (ECR) technique was used for the D^* and k^* of electrode materials, and the green cathode powders were dry-pressed and then sintered at 1175 °C for 10 h to obtain the dense bar samples. An X-ray photoelectron spectrometer (XPS) (Thermo Scientific K-Alpha) was employed to identify elements in samples. Inductively coupled plasma (ICP) analysis (Agilent 5110) was conducted to elucidate the equimolarity of a high-entropy perovskite cathode. The iodine titration method was used to examine the oxygen vacancy concentrations of the samples, and the details of iodine titration have been reported.[35, 36] In this work, 0.8 g $PBSLC_{25}C$ powders were dry-pressed in a bar model (with the length of 20 mm and the width of 6 mm) at a pressure of 1 MPa, and then sintered at 1150 °C for 10 h in air to obtain the dense bars for thermal expansion coefficient (TEC) measurements. The thermal expansion coefficient (TEC) of the sample was tested by the equipment of Netzsch DIL 402 in air from room temperature to 1000 °C at the heating rate of 20 °C min^{-1}. The CO_2-temperature programmed desorption (TPD) was conducted by a mass spectrometer (HPR-20EGA), and the samples were all experienced by the process of pre-treatments under the 10% CO_2/air atmosphere. Raman spectroscopy (RenishawRM1000) was conducted by a wavelength of 514 nm to detect the carbonate or/and deposited carbon on the electrode surface. The electrochemical impedance of the electrodes was measured in the air, the air with different $p_{CO2,}$ or different p_{O2} by a potentiostat (PARSTAT MC 200), respectively. For tests of SOFC performance, the cells were sealed onto the alumina tube with ceramic paste (AREMCO 552), and then put inside the furnace and heated to the needed temperatures at the heating rate of 3 °C min^{-1}. the fuel electrode was flowed with humidified hydrogen (3% H_2O) at the rate of 60 mL min^{-1}, while the air electrode was exposed to air and air containing 1%, 5%, and 10% CO_2 at the total rate of 100 ml min^{-1}. The air and CO_2 gases were accurately controlled by two flow meters (KMG3-21) at the specific ratios of 1%, 5%, or 10%, respectively. The frequency range for all impedance measurements was between 100 mHz and 10 kHz with an AC amplitude of 10 mV. The I-V-P curves and EIS of single cells were tested using a potentiostat (PARSTAT MC 200) at 700-800 °C, and electrochemical impedance spectroscopic (EIS) measurements of symmetrical cells were also performed using a potentiostat (PARSTAT MC 200) at 650-850 °C.

2.4. Computational methods

Periodic density functional theory (DFT) calculations were carried out using the Vienna ab initio simulation package (VASP)[37, 38] to examine the enhanced ORR activity and the CO_2 tolerance of high-entropy $PBSLC_{25}C$. The projector augmented wave (PAW)[39] method and the Perdew-Burke-Ernzerhof (PBE)[40] exchange-correlation functional were used with a kinetic energy cutoff of 415 eV. In particular, to accurately describe the strongly correlated electronic states of the Co cation at the B site,[41] the Hubbard U correction with the U_{eff} value of 4.0 eV was applied.[42] The detailed computational methods are available in **Supplementary Note 1**.

3. Results and discussion

3.1. Structural analysis of the Ca-rich high-entropy $PBSLC_{25}C$

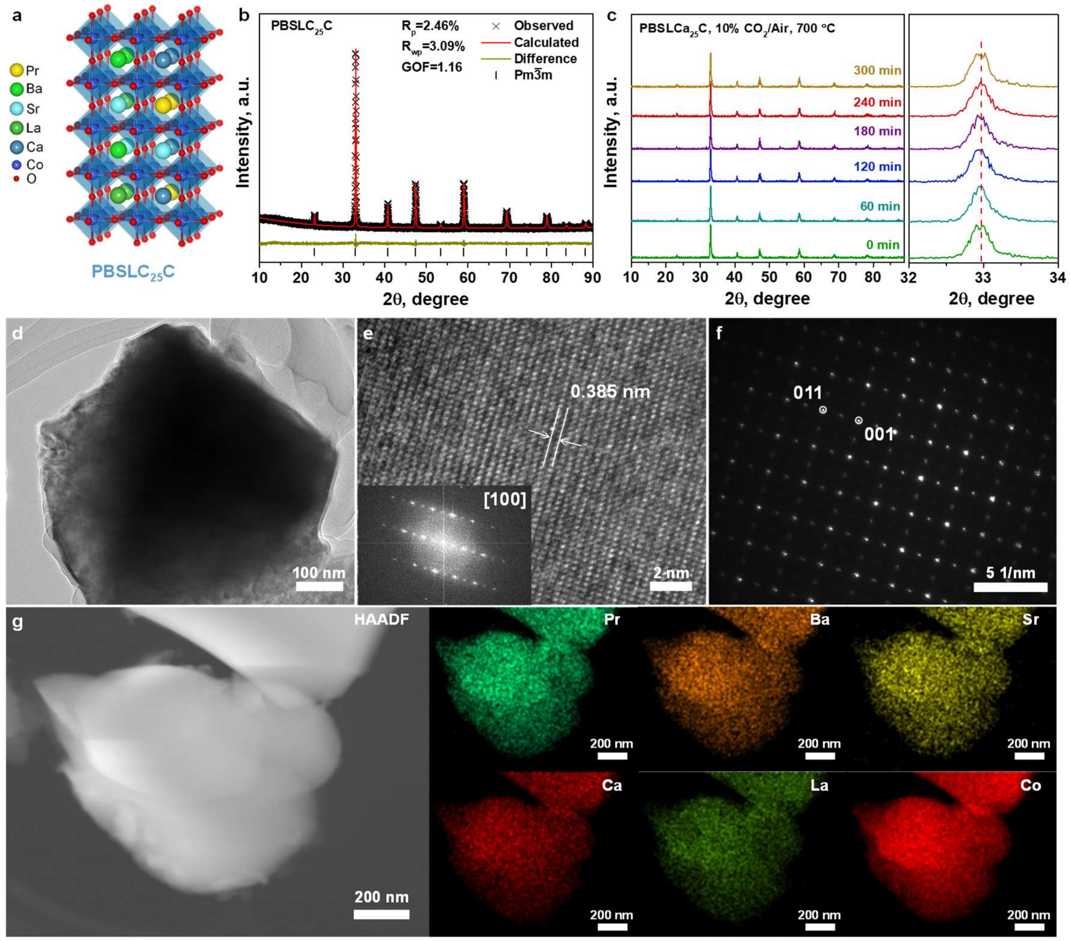

Figure 1. Crystalline structure of PBSLC$_{25}$C powders. (a) Schematic of the non-equimolar PBSLC$_{25}$C. **(b)** Refined XRD pattern of as-synthesized PBSLC$_{25}$C powders. **(c)** In-situ XRD patterns of PBSLC$_{25}$C powders in the air containing 10% CO$_2$ at 700 °C and different processing times. **(d)** STEM and **(e)** high-resolution TEM images of a PBSLC$_{25}$C grain. The inset is the fast Fourier transform (FFT) pattern in (e). **(f)** A SAED image of the PBSLC$_{25}$C grain. **(g)** High-angle annular dark-field STEM image combined with the EDS mapping of the PBSLC$_{25}$C grain.

Fig. 1a schematically depicts the structure of the high-entropy PBSLC$_{25}$C. The actual atomic ratio of as-synthesized PBSLC$_{25}$C was validated near the nominal stoichiometric ratio by inductively coupled plasma mass spectrometry (ICP-MS) (**Supplementary Table 1**). Shown in **Fig. 1b** is the room-temperature (RT) X-ray diffraction (XRD) pattern of as-synthesized PBSLC$_{25}$C powders sintered at 1000 °C for 5 h. The refinement demonstrated that Ca-rich PBSLC$_{25}$C has a cubic perovskite structure with the space group of $Pm\bar{3}m$ and lattice parameters of a=3.8351(8) Å (a fitted factor of 1.16), similar to the original PBSLCC (space group of $Pm\bar{3}m$, a=3.8500 Å) (**Supplementary Table 2**).[31] The phase structural variations on the PBSLC$_{25}$C were evaluated by high-temperature XRD (HT-XRD) from RT to 800 °C (**Fig. S1**). The distinctive perovskite peaks at 31-35° shifted towards the low angles without the appearance of secondary phases at elevated temperatures to 800 °C. To further examine the structural stability of PBSLC$_{25}$C, an in-situ XRD was performed in air containing 10% CO$_2$ at 700 °C with intervals of 60 min (**Fig. 1c**). No peaks representing carbonates and apparent shifts were observed during each poisoning processing time for a total of 300 min, confirming the excellent structural tolerance of PBSLC$_{25}$C against CO$_2$ contaminant. Shown in **Fig. 1d** is the scanning transmission microscopy (STEM) image of the PBSLC$_{25}$C grain. The space distance between the adjacent bright planes is about 3.85 Å, consistent with the (100) plane of PBSLC$_{25}$C from the XRD results (**Fig. 1e**). The inset (**Fig. 1e**) is the fast Fourier transform (FFT) based on the high-resolution TEM image, and the marked diffraction spots correspond to the planes of [011] and [001], as shown in the selected area electron diffraction (SAED) image of the PBSLC$_{25}$C (**Fig. 1f**). The element distributions of PBSLC$_{25}$C were also examined by the high-angle annular dark-field (HAADF) STEM and X-ray energy dispersive spectrum (EDS) (**Fig. 1g**). The six elements of Pr, Sr, Ba, Ca, La, and Co are homogeneously distributed in the selected high-entropy particle without Ca cation enrichments.

3.2. Electrochemical performance and theoretical interpretation of the highly active PBSLC$_{25}$C electrode

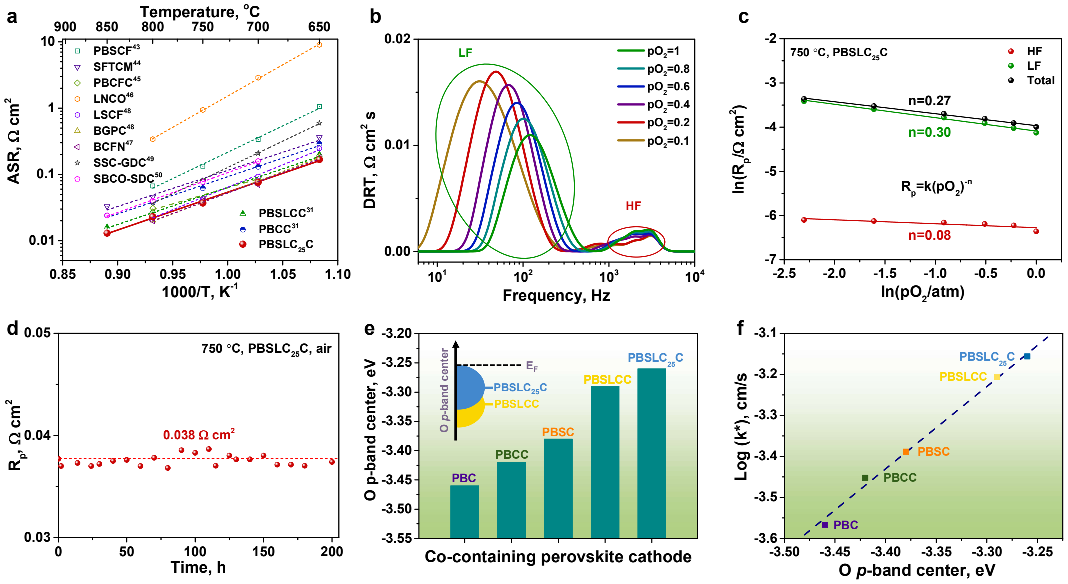

Figure 2. Electrochemical performance and theoretical interpretation of the highly active PBSLC$_{25}$C electrode. (a) Arrhenius plots of ASRs of symmetrical cells with the PBSLC$_{25}$C electrode in comparison with many other reported electrode materials, including PBSCF,[43] SFTCM,[44] PBCFC,[45] LNCO,[46] BCFN,[47] BGPC,[48] SSC-GDC,[49] SBCO-SDC,[50] LSCF,[48] PBSLCC,[31] and PBCC[31] composites; **(b)** DRT analysis of the PBSLC$_{25}$C electrode measured at different oxygen partial pressures (p_{O2}) at 750 °C; **(c)** Dependence of polarization resistance (R_p) of PBSLC$_{25}$C at different frequency ranges and 750 °C as functions of p_{O2}; **(d)** Time dependence of R_p values of the PBSLC$_{25}$C electrode at 750 °C in air; **(e)** Comparison of the bulk O *p*-band center of PBC, PBCC, PBSC, PBSLCC, and PBSLC$_{25}$C calculated using the hybrid HSE06 functional with the structures optimized at PBE + U; **(f)** Linear correlation of the experimental surface exchange coefficients (k*) measured at 700 °C as a function of the bulk O *p*-band center for PBC, PBCC, PBSC, PBSLCC, and PBSLC$_{25}$C.

Shown in **Fig. S2** are the electrochemical impedance spectra (EIS) of the PBSLC$_{25}$C cathode determined by symmetrical cells with a configuration of PBSLC$_{25}$C|LSGM|PBSLC$_{25}$C in ambient air at 650-850 °C. The LSGM electrolyte is a typical oxygen ion-conducting electrolyte with excellent chemical and thermal compatibility,[51] which was applied to evaluate the electrochemical performance of electrodes using symmetrical cells in this work. Herein, LSGM was used for the symmetric cells to avoid using a protective GDC barrier layer. The thermal expansion coefficient (TEC) of the $PBSLC_{25}C$ above 500 °C is 25.1×10^{-6} K^{-1}, and that below 500 °C is 18.1×10^{-6} K^{-1}. The relative high TEC above 500 °C may be ascribed to the thermal reduction of cobalt ions and thermally activated transition in the spin state of the Co *d*-orbital electrons.[4] The relatively high TEC could be reduced by mixing the cathodes with electrolyte phases[52] or negatively-thermal expansion phases.[4] The interfacial R_p value (0.037 Ω cm^2 at 750 °C in air) of $PBSLC_{25}C$ is slightly lower that (0.043 Ω cm^2 at 750 °C in air) of PBSLCC at the same condition, which is also comparable to those of the high-performance cathodes with good stabilities reported recently (**Fig. 2a and Supplementary Table 3**), including $PrBa_{0.5}Sr_{0.5}Co_{1.5}Fe_{0.5}O_{5+\delta}$ (PBSCF),[43] $SrFe_{0.25}Ti_{0.25}Co_{0.25}Mn_{0.25}O_{3-\delta}$ (SFTCM),[44] $PrBaCo_{2/3}Fe_{2/3}Cu_{2/3}O_{5+\delta}$ (PBCFC),[45] $LaNi_{0.6}Co_{0.4}O_{3-\delta}$ (LNCO),[46] $Ba_{0.9}Co_{0.7}Fe_{0.2}Nb_{0.1}O_{3-\delta}$ (BCFN),[47] $Ba_{0.8}Gd_{0.8}Pr_{0.4}Co_2O_{6-\delta}$ (BGPC),[48] $Sm_{0.5}Sr_{0.5}CoO_{3-\delta}$ (SSC)-GDC,[49] $SmBaCo_2O_{5+\delta}$ (SBCO)-SDC,[50] $(La_{0.6}Sr_{0.4})_{0.95}Co_{0.2}Fe_{0.8}O_{3-\delta}$ (LSCF),[48] $Pr_{0.2}Ba_{0.2}Sr_{0.2}La_{0.2}Ca_{0.2}CoO_{3-\delta}$ (PBSLCC),[31] and PBCC[31] composites. The higher electrocatalytic activity of the $PBSLC_{25}C$ cathode may result from more oxygen vacancy concentrations at room temperature, as obtained by the typical iodine titration measurement (**Fig. S4**). The surface kinetics of the $PBSLC_{25}C$ cathode were further investigated via electrochemical impedances tested under different oxygen partial pressures (p_{O2}), and then the impedances were analyzed by the distribution of relaxation time (DRT) (**Fig. S5** and **Fig. 2b**). According to the resistance contributions from each frequency, the electrode reaction at LF of total charge transfer (i.e., $O_{ads} + 2e^- + V_O^{\cdot\cdot} \rightarrow O_O^{\times}$) was highly associated with the key rate-limiting electrochemical step, as judged by the n value (reaction order) from the equation of $R_p=k(pO_2)^{-n}$ (**Fig. 2c**, **Supplementary Note 2**).[44, 53, 54] A relatively stable R_p of 0.037 Ω cm^2 was achieved within the stability test of 200h in air at 750 °C (**Fig. 2d** and **Fig. S6**). The enhanced activity is attributed to the faster kinetics of surface oxygen exchange (k^*) and a higher coefficient of bulk oxygen transfer (D^*), compared to those of the PBSLCC reported recently (**Fig. S7**, **Supplementary Table 3**).

As shown in **Fig. 2e**, we further carried out density functional theory (DFT) calculations to elucidate the enhanced ORR activity and CO_2 tolerance of the high-entropy perovskite of $PBSLC_{25}C$. The bulk structures[51] used in this study are summarized in **Supplementary Table 4** and **Fig. S8**. As schematically depicted in **Fig. 1a**, additional Ca doping was applied in the equimolar high-entropy PBSLCC structure[51] by adding one more Ca ion to support the experimental observation, resulting in non-equimolar $PBSLC_{25}C$. **Fig. S9** illustrates the strong hybridization of cations in the Co ions with oxygen of PBSLCC and $PBSLC_{25}C$ using the hybrid HSE06 functional.[55] Then, the bulk O *p*-band center, widely used as a descriptor for the rational design of SOFC cathode materials[13, 56, 57], was calculated as compiled in **Supplementary Table 5**. It was found that more Ca doping in PBSLCC slightly shifts the bulk O *p*-band center to the Fermi level (–3.29 eV versus –3.26 eV). Moreover, we also examined that of PBSC as it was used for the comparative study of CO_2 tolerance by more Ca doping in the perovskite. **Fig. 2e** exhibits the apparent correlation of the perovskite-structured cathode materials, theoretically supporting the enhanced ORR activity[13, 56, 57] of the high-entropy $PBSLC_{25}C$ cathode compared to PBC, PBCC, PBSC, and PBSLCC. More specifically, to evaluate the A-site entropy tuning of PBSLCC by additional Ca doping, we calculated the adsorption energy of oxygen by placing superoxo-like species[58] in the most stable, reactive CoO-terminated (001) plane (**Supplementary Table 5** and **Fig. S10**). Its trend aligns well with the O *p*-band behavior (**Fig. S10f**). In addition, as shown in **Fig. 2f**, we also confirmed that the first-principles-based O *p*-band centers are linearly correlated with their surface exchange coefficients (k^*) measured in this study (**Fig. S11**) and available in the literature.[51] We assumed that the additional Ca doping in equimolar, high-entropy PBSLCC may weaken oxygen adsorption to reach its maximum ORR activity by increasing the kinetics of diffusion and desorption processes.[59]

3.3. Robustness of the high-entropy PBSLC$_{25}$C electrode tested in air with CO$_2$

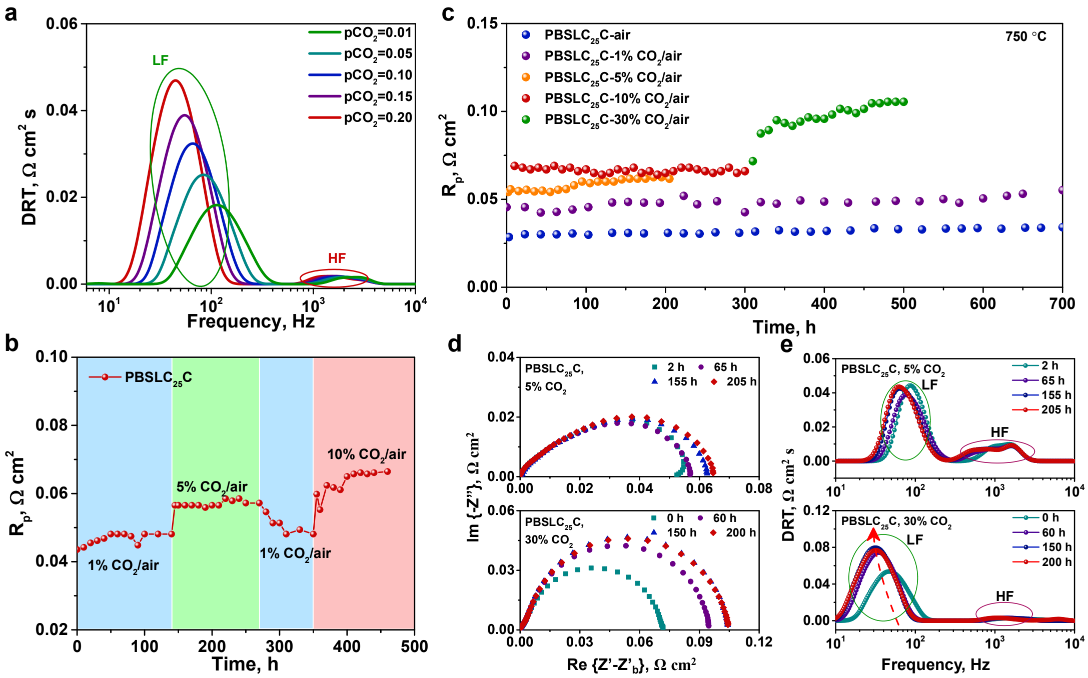

Figure 3. Durability of PBSLC$_{25}$C in air with various CO$_2$ concentrations. (a) DRT analysis of the PBSLC$_{25}$C electrode measured at different p_{CO2} at 750 °C; **(b)** Regenerative R$_p$ stability of PBSLC$_{25}$C when being switched among various CO$_2$ concentrations of 1%, 5%, and 10% at 750 °C; **(c)** Long-term durability of the PBSLC$_{25}$C cathode in air with different concentrations of CO$_2$ tested at 750 °C under OCV conditions; **(d)** EIS and **(e)** the corresponding DRT of the PBSLC$_{25}$C electrode tested at different times under different CO$_2$ concentrations: 5% (top) and 30% (bottom).

Apart from high electrocatalytic performance, the electrode durability against contaminants (such as CO$_2$) has attracted increasing concerns towards SOFC commercialization. When exposed to 1% CO$_2$/99% air, the R$_p$ of the PBSLC$_{25}$C electrode reached up to 0.039 Ω cm^2 at 750 °C (**Fig. S12**), slightly higher than that (0.032 Ω cm^2 at 750

°C) of the $PBSLC_{25}C$ electrode in the air. The electrode surface kinetics of the $PBSLC_{25}C$ electrode under the air containing CO_2 condition was investigated by the DRT analysis on the electrochemical impedances (**Fig. 3a** and **Fig. S13**). It is found that the degradation on the kinetics of the electrode surface reaction did occur due likely to the CO_2 poisoning for ORR on the electrode surface. Based on the associated equation of $R_p=k(p_{CO2})^m$, m=0.12 for the peak at HF (**Figure S14**) may indicate the transfer of O^{2-} through the LSGM electrolyte.[60, 61] The gas-associated (CO_2 and/or O_2) diffusion processes of adsorption and dissociation ($m_{LF}=0.29$, dependence on the variations of p_{CO2})[62, 63] may be urgently in need of optimization when exposed to the air with CO_2 (**Fig. S15**, **Supplementary Note 3**). The excellent regenerative R_p stability of $PBSLC_{25}C$ was verified by the well-recovered impedances, such as 0.044 Ω cm^2 in air/1% CO_2 (the first test for 140 h), 0.057 Ω cm^2 in air/5% CO_2 (the second test for 130 h), and then 0.048 Ω cm^2 in air/1% CO_2 (the third test for 80 h) (**Fig. 3b**, **Supplementary Note 4**). Finally, $PBSLC_{25}C$ still showed the remarkable R_p stability of ~0.066 Ω cm^2 in air containing 10% CO_2 for the fourth stability test of 110 h (total 460 h). Comparatively, the R_p value of the PBSC electrode dramatically increased after the test with only 50 h-exposure in air/5% CO_2 and air/ 10% CO_2. The R_p of PBSC electrode is not recoverable to the pristine values (two-fold increase) even in air, much worse than the regenerative performance of the Ca-rich $PBSLC_{25}C$ electrode (**Fig. S15**). The SEM images of the $PBSLC_{25}C$ and PBSC electrodes after the 50-h exposure in air/5% CO_2 at 750 °C were shown in **Fig. S16**. It is shown that the surface of the PBSC electrode was covered by abundant carbonate nanoparticles, rougher than that of the $PBSLC_{25}C$ electrode and differing from the original PBSC.

Shown in **Fig. 3c** is the summary of the durability of the $PBSLC_{25}C$ electrode in air with various concentrations of CO_2. The R_p of the $PBSLC_{25}C$ electrode exceptionally remained stable at 0.034 and 0.045 Ω cm^2 when exposed to the air and the air containing 1% CO_2, respectively. Even when the CO_2 concentration increased to 5%, 10%, and 30%, the R_p of the $PBSLC_{25}C$ electrode increased at a relatively low rate. As comparisons, the R_p of high-entropy

PBSLCC and Sr-free PBCC electrodes increased from 0.100 to 0.114 Ω cm^2 and from 0.133 to 0.164 Ω cm^2 in the air containing 10% CO_2 at 750 °C during the 100 h's operation, respectively (**Fig. S17a**). We further investigated the electrochemical reaction evolutions of each process of the electrode impedances as a function of operation time using DRT (**Fig. 3d** and **3e**). Similar to the above analyses, it is found that at least two processes in the frequency domain could be assigned to the electrode reaction (**Fig. 3e**), such as mass and/or gas transfer at LF, and ion and/or electron transfer at HF. According to the DRT analysis, the increase of R_p could be contributed to the sluggish surface electrode reaction of the PBSLCC and PBCC electrodes under the CO_2 poisoning condition (10% CO_2/90% air) (**Fig. S17b and S17c**). A down-shifting of a specific process on the characteristic frequency may suggest the degradation in the kinetics of the electrode process (e.g., surface reaction) due to the contaminant poisoning. The characteristic frequency of the LF peaks can be observed to shift towards a lower frequency when the $PBSLC_{25}C$ electrode was exposed to the air with CO_2 concentration varied from 5 to 30% (**Fig. 3e**). The integral impedance apparently increased with prolonged exposing time under a higher concentration of CO_2 (e.g., 30%), strongly suggesting that high-concentration CO_2 indeed blocked the active sites for ORR and then hindered the process of the gas and mass transfer on the electrode surface (as determined by continuously increasing resistances at LF). However, when the operating conditions were in air containing 5% and 10% CO_2, the resistance of the gas and mass transfer process (LF) maintained relatively stable simultaneously with the fixed characteristic frequency, an indication of the durable high-entropy and A-site Ca-rich structure of the $PBSLC_{25}C$ cathode against contaminant poisoning up to 10% CO_2.

3.4. Single cells performance and understandings of the CO_2 tolerance

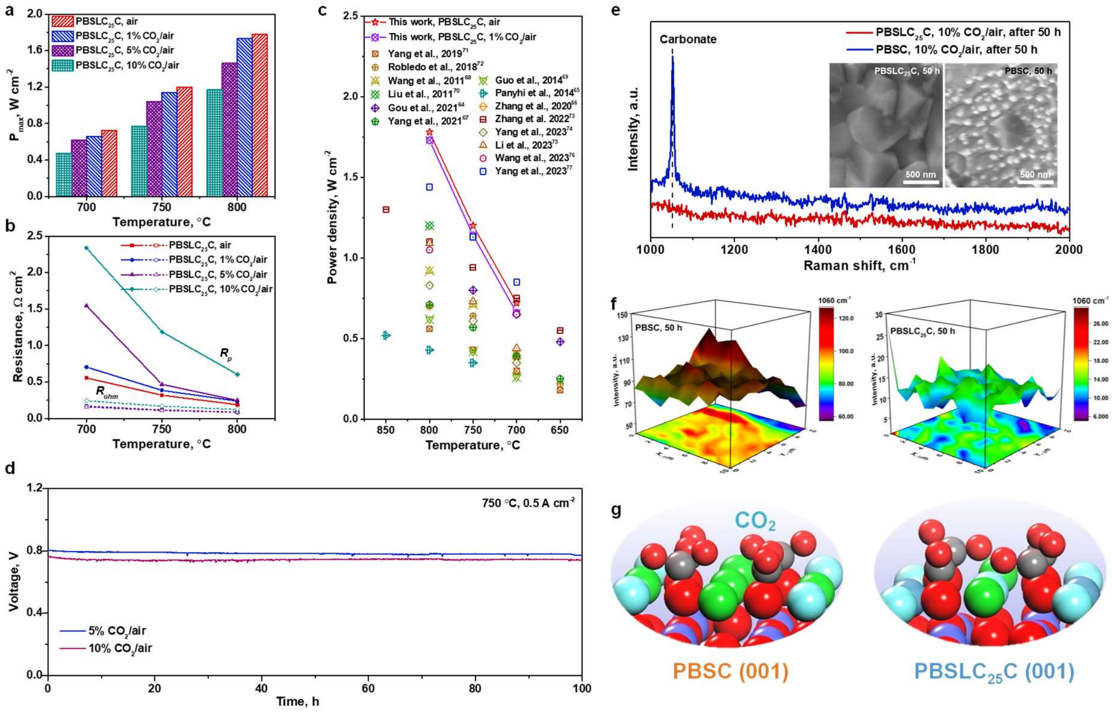

Figure 4. Electrochemical performance of single cells with PBSLC$_{25}$C cathode in air with CO$_2$, and understandings of high-entropy stabilized surface structure. (a) Comparisons on the peak power densities (P$_{max}$) and **(b)** resistances (R$_p$ and R$_{ohm}$) of the cells with the PBSLC$_{25}$C cathode in air containing different concentrations of CO$_2$ at 700-800 °C; **(c)** Performance comparisons of the cell with the PBSLC$_{25}$C cathode with different cathode materials,[64-77] PBSLC$_{25}$C operating at 700-800 °C in air with/without 1% CO$_2$; **(d)** Short-term operational stabilities of the cells with the PBSLC$_{25}$C cathode at 750 °C under a current density of 0.5 A cm^{-2} in air containing 5% and 10% CO$_2$; **(e)** Raman spectra of PBSLC$_{25}$C and PBSC dense membranes after exposure to air with 10% CO$_2$ for 50 h; insets are SEM (surface) of the as-treated PBSLC$_{25}$C (left) and PBSC (right) membranes in air containing 10% CO$_2$ for 50 h; **(f)** Raman mapping of SrCO$_3$ (peaks at 1060 cm^{-1}) on the PBSLC$_{25}$C (right) and PBSC (left) dense membranes after exposure to air containing 10% CO$_2$ for 50 h at 750 °C; and **(g)** Illustration of representative CO$_2$ adsorption on A-site cation terminated PBSC(001) (top) and PBSLC$_{25}$C(001) (bottom) with θ = 1.0 ML (monolayer);

To evaluate the ORR activity and CO_2-tolerance of the $PBSLC_{25}C$ cathode under realistic operating conditions, a single cell with a configuration of Ni-YSZ anode support layer, Ni-YSZ anode functional layer, YSZ electrolyte (~7 μm), GDC barrier layer (~3 μm), and porous $PBSLC_{25}C$ cathode was constructed (**Fig. S18**). The GDC barrier layer was utilized to prevent the adverse phase reactions between the YSZ electrolyte and $PBSLC_{25}C$ electrode, as checked by the XRD patterns (**Fig. S19**). Not surprisingly, the performance of the cell with the $PBSLC_{25}C$ cathode was indeed impacted by the concentrations of CO_2. For instance, the P_{max} of 1.20, 1.14, 1.04, and 0.77 W cm^{-2} can be delivered at 750 °C when exposed to the ambient air and the air with 1%, 5%, and 10% CO_2, respectively (**Fig. 4a,** and **Figure S20-S23**). Based on the comparisons of the corresponding resistances (R_{ohm}, and R_p) in **Fig. 4b**, the main contribution to the cell resistance increase is the R_p change of the cathode in the air with different CO_2 concentrations. The ohmic resistances (R_{ohm}) of the single cells had shown an insignificant difference. For instance, the R_{ohm} of the single cells were 0.12, 0.12, 0.12, and 0.18 Ω cm^2 at 750 °C in air with 0%, 1%, 5%, and 10% CO_2 respectively. The slight increase in R_{ohm} may be caused by the formation of insulating phases in the cathode/electrolyte interface or the degradation of current collector layer.[78, 79] The R_p values of the cell with the $PBSLC_{25}C$ cathode dramatically increased from 0.39 to 1.19 Ω cm^2 with the CO_2 concentrations of 1% to 10% at 750 °C, suggesting the necessity of the improvement on the CO_2-tolerance for the developed cathodes towards actual commercialization. It is comparatively found that the P_{max} of the cell with the $PBSLC_{25}C$ cathode can surpass most of the previously reported high-performance SOFCs, even in the air containing CO_2 (1%) contaminant (as summarized in **Fig. 4c** and **Supplementary Table 6**).[64-77] To demonstrate the excellent CO_2-tolerance of the high-entropy $PBSLC_{25}C$ cathode (**Supplementary Note 5**), we further conducted the short-term stabilities of the cell with the $PBSLC_{25}C$ cathode at a current density of 0.5 A cm^{-2} at 750 °C using the humidified H_2 (~3% H_2O) as a fuel and the air containing 5% and 10% CO_2 as an oxidant (**Fig. 4d**). As clearly shown, the cell with the PBSLC$_{25}$C cathode delivered a stable output under the conditions containing high-concentration CO$_2$, exhibiting the excellent poisoning tolerance against 5% and 10% CO$_2$, which are consistent with the above symmetrical cell stabilities in **Fig. 3c**. The short-term stability and EIS of the single cell with the PBSLC$_{25}$C electrode were measured under different current densities of 0.25, 0.5, 0.75 and 1.0 A cm^{-2} in air containing 5% CO$_2$ at 750 °C (**Fig. S24**). The cell with the PBSLC$_{25}$C electrode can maintain relatively stable voltage curves under the different applied current densities (**Fig. S24a**). The total resistance of the cell with PBSLC$_{25}$C electrode were 0.54, 0.31, 0.30, 0.29, and 0.28 Ω cm^2 at the current densities of 0 (OCV condition), 0.25, 0.5, 0.75, and 1.0 A cm^{-2}, respectively (**Fig. S24b**). According to the DRT analysis (**Fig. S24c**), peak 4 (P4) at low frequency was more significantly affected by the applied current densities when the electrode was exposed in the air containing 5% CO$_2$, which may be corresponding to the gas-associated (CO$_2$ and/or O$_2$) diffusion processes on the high-entropy electrode surface.

To gain a deeper understanding of the durable surface properties of the high-entropy PBSLC$_{25}$C, we have fabricated dense PBSLC$_{25}$C and PBSC membranes to investigate the surface interactions within the 50 h's exposure in air containing 10% CO$_2$ using Raman spectroscopy. Shown in **Fig. 4e** are the Raman spectra obtained from the PBSLC$_{25}$C and PBSC membranes after exposed to air containing 10% CO$_2$ at 750 °C for 50 h. The as-treated PBSC showed an apparent peak near 1060 cm^{-1}, highly associated with carbonates[11] (e.g., SrCO$_3$ or/and BaCO$_3$) (**Fig. S25**, **Supplementary Note 6**). However, the Raman spectra of the PBSLC$_{25}$C membrane were featureless after the same treatment, verifying the high-entropy structure can inhibit the surface element (Sr or/and Ba) segregation and be finally inert for the formation of carbonates even when the CO$_2$ concentration reaches up to 10%. The surface of the dense PBSC membrane (inset right) was covered with many nanoparticles after exposure to air/10%CO$_2$, while the dense PBSLC$_{25}$C membrane (inset left) kept a smooth surface (**Fig. 4e**, inset). To further investigate the information of the carbonate formed on the membrane surface, Raman mapping of the carbonate peak at 1060 cm^{-1} was conducted within a grid of 10 μm × 10 μm, as demonstrated in **Fig. 4f**. The high intensity (red region) of carbonate (1060 cm^{-1}) was considerably observed on the surface of PBSC after 50 h exposure to air/10% CO_2, and the PBSC membrane became much rougher, as obtained from the three-dimensional pattern in **Fig. 4f** (left). However, the $PBSLC_{25}C$ membrane exhibited the low intensity (blue region) of carbonate (1060 cm^{-1}) with a relatively flat surface (**Fig. 4f**, right), indicating that the high-entropy $PBSLC_{25}C$ membrane is much more robust against CO_2 compared to the PBSC membrane via the effective restraining of element segregation toward the electrode surface. Furthermore, an evolution on the surface structure of $PBSLC_{25}C$ and PBSC before and after exposure to air containing 10% CO_2 for 50 h was examined by Sr 3d X-ray photoelectron spectroscopy (XPS) curves (**Fig. S26** and **Supplementary Note 7**). According to the Ba $3d_{5/2}$ and Ca 2p XPS curves, the surface Ba contents of the PBSC were higher than that of the $PBSLC_{25}C$ under the retreatments of 10% CO_2/air at 750 °C for 50 h, and the Ca contents in the high-entropy $PBSLC_{25}C$ structure could maintain well during the same condition (**Fig. S27**). The more stable surface of high-entropy $PBSLC_{25}C$ may lead to the lower ohmic and polarization resistances, and enhanced cell stability. The treated $PBSLC_{25}C$ exhibited more oxygen vacancy concentrations for ORR activity compared to the PBSC sample (**Fig. S28** and **Supplementary Note 8**). The high-entropy $PBSLC_{25}C$ possessed the lower started desorption temperatures of CO_2 and less CO_2 desorption amount compared to PBSC, as verified by CO_2-TPD for the powders after CO_2 pre-treatments (**Fig. S29**, **Supplementary Note 9**). These results strongly indicated that high-entropy $PBSLC_{25}C$ with A-site Ca enrichment has an excellent structural tolerance on 10% CO_2, performing as a weaker bonding capability with CO_2 and robust surface against the carbonate formation.

Then, similar to previous studies,[80-82] the outstanding CO_2 tolerance of high-entropy $PBSLC_{25}C$ was theoretically investigated by calculating CO_2 adsorption energies in the (001) plane and compared with Sr-doped PBSC(001) (**Fig. S30**). We initially verified that the CO_2

adsorption on the catalytically active CoO-terminated surface is weaker bound than on A-cation-containing surfaces (**Supplementary Table 7**). Then, we considered only A-cation-containing surfaces, similar to our previous study[80], by assuming that the peak at 1,060 cm^{-1} shown in **Fig. 4e** is associated with the carbonate formation resulting from segregated A-site cations from PBSC (i.e., $SrO + CO_2 \rightarrow SrCO_3$). As schematically displayed in **Fig. 4g** and **S30**, the adsorption energy calculations support the experimental findings that the CO_2 adsorption on PBSLC$_{25}$C is weaker than PBSC (–0.55 eV versus –0.76 eV), which hinders the carbonate formation and maintains the excellent fuel cell performance. We theoretically verified that the non-equimolar high-entropy perovskite PBSLC$_{25}$C exhibits outperformed ORR activity using the bulk O *p*-band center and CO_2 tolerance by examining CO_2 adsorption energies.

4. Conclusions

In summary, a Ca-rich high-entropy perovskite PBSLC$_{25}$C cathode with excellent electrocatalytic ORR activity and CO_2 tolerance was successfully engineered and investigated under the actual cell operating conditions in both symmetrical and full cells. The PBSLC$_{25}$C cathode exhibited a highly active electrocatalytic performance and a remarkably low R_p of 0.032 Ω cm^2 at 750 °C. The analysis of the R_p durability combined with DRT suggests that the high-entropy PBSLC$_{25}$C can enhance the surface robustness against CO_2 poisoning, leading to highly optimized gas diffusion and surface exchange on the electrode surfaces. When applied in a full cell, the cells with the PBSLC$_{25}$C cathode performed exceptional peak power densities of 1.2, 1.14, 1.04, and 0.77 W cm^{-2} in ambient air, and air with 1%, 5%, and 10% CO_2, respectively, at 750 °C. Excellent CO_2-tolerance with no noticeable degradations was demonstrated in air containing 5% and 10% CO_2. The high-entropy PBSLC$_{25}$C cathode could diminish carbonate formation and thus stabilize the perovskite structure for maintaining excellent ORR activities, as disclosed by the Raman spectroscopy and DFT calculations. Our novel high-performance electrode design strategy of high-entropy perovskites via the A-site

Ca-rich can be effectively applied not only for highly CO_2-tolerance cathodes in SOFCs but also for CO_2 electrolysis, membrane reactors, oxygen separation membranes, and gas sensors.

Declaration of Competing Interest

The authors declare that they have no known competing financial interests or personal relationships that could have appeared to influence the work reported in this paper.

CRediT authorship contribution statement

Fan He: Investigation, Data curation, Visualization, Writing-original draft. **Feng Zhu:** Investigation. **Kang Xu:** Investigation. **Yangsen Xu:** Investigation. **Dongliang Liu:** Investigation. **Guangming Yang:** Data curation. **Kotaro Sasaki:** Writing-review & editing. **YongMan Choi:** Software, Resources, Writing-review & editing. **Yu Chen:** Conceptualization, Writing-review & editing, Project administration, Funding acquisition.

Acknowledgments

This work is financially supported by the Introduced Innovative R&D Team of Guangdong (Grant No. 2021ZT09L392), the National Natural Science Foundation of China (Grant Nos. 22179039 and 22005105), and the Pearl River Talent Recruitment Program (Grant No. 2019QN01C693). Computational studies were supported by the National Science and Technology Council (NSTC Grant No. 110-2221-E-A49-017-MY3 and 111-2221-E-A49-003-MY3) and the National Center for High-performance Computing (NCHC), Taiwan. DFT calculations were performed using the resources of the Center for Functional Nanomaterials, which is a U.S. DOE Office of Science Facility, at Brookhaven National Laboratory under Contract No. DE-SC0012704.

Appendix A. Supporting information

Supplementary data associated with this article can be found in the online version at

References

[1] C. Duan, R.J. Kee, H. Zhu, C. Karakaya, Y. Chen, S. Ricote, A. Jarry, E.J. Crumlin, D. Hook, R. Braun, Highly durable, coking and sulfur tolerant, fuel-flexible protonic ceramic fuel cells, Nature, 557 (2018) 217-222.

[2] W. Bian, W. Wu, B. Wang, W. Tang, M. Zhou, C. Jin, H. Ding, W. Fan, Y. Dong, J. Li, Revitalizing interface in protonic ceramic cells by acid etch, Nature, 604 (2022) 479-485.

[3] H. Xie, Z. Zhao, T. Liu, Y. Wu, C. Lan, W. Jiang, L. Zhu, Y. Wang, D. Yang, Z. Shao, A membrane-based seawater electrolyser for hydrogen generation, Nature, (2022) 1-6.

[4] Y. Zhang, B. Chen, D. Guan, M. Xu, R. Ran, M. Ni, W. Zhou, R. O'Hayre, Z. Shao, Thermal-expansion offset for high-performance fuel cell cathodes, Nature, 591 (2021) 246-251.

[5] F. He, Y. Zhou, T. Hu, Y. Xu, M. Hou, F. Zhu, D. Liu, H. Zhang, K. Xu, M. Liu, An efficient high‐entropy perovskite‐type air electrode for reversible oxygen reduction and water splitting in protonic ceramic cells, Advanced Materials, (2023) 2209469.

[6] Z. Zhan, S.A. Barnett, An octane-fueled solid oxide fuel cell, Science, 308 (2005) 844-847.

[7] E.P. Murray, T. Tsai, S.A. Barnett, A direct-methane fuel cell with a ceria-based anode, Nature, 400 (1999) 649-651.

[8] B. Qian, Y. Zhang, X. Hou, D. Bu, K. Zhang, Y. Lan, Y. Li, S. Li, T. Ma, X.M. Song, A Dual Photoelectrode Photoassisted Fe‐Air Battery: The Photo‐Electrocatalysis Mechanism Accounting for the Improved Oxygen Evolution Reaction and Oxygen Reduction Reaction of Air Electrodes, Small, 18 (2022) 2103933.

[9] H. Zhang, K. Xu, F. He, Y. Zhou, K. Sasaki, B. Zhao, Y. Choi, M. Liu, Y. Chen, Surface Regulating of a Double‐Perovskite Electrode for Protonic Ceramic Fuel Cells to Enhance Oxygen Reduction Activity and Contaminants Poisoning Tolerance, Advanced Energy Materials, 12 (2022) 2200761.

[10] M. Shao, Q. Chang, J.-P. Dodelet, R. Chenitz, Recent advances in electrocatalysts for oxygen reduction reaction, Chemical reviews, 116 (2016) 3594-3657.

[11] Y. Chen, S. Yoo, Y. Choi, J.H. Kim, Y. Ding, K. Pei, R. Murphy, Y. Zhang, B. Zhao, W. Zhang, A highly active, CO_2-tolerant electrode for the oxygen reduction reaction, Energy & Environmental Science, 11 (2018) 2458-2466.

[12] Z. Liu, Z. Tang, Y. Song, G. Yang, W. Qian, M. Yang, Y. Zhu, R. Ran, W. Wang, W. Zhou, High-entropy perovskite oxide: A new opportunity for developing highly active and

durable air electrode for reversible protonic ceramic electrochemical cells, Nano-Micro Letters, 14 (2022) 217.

[13] Y.-L. Lee, J. Kleis, J. Rossmeisl, Y. Shao-Horn, D. Morgan, Prediction of solid oxide fuel cell cathode activity with first-principles descriptors, Energy & Environmental Science, 4 (2011) 3966-3970.

[14] F. Calle-Vallejo, O.A. Díaz-Morales, M.J. Kolb, M.T. Koper, Why is bulk thermochemistry a good descriptor for the electrocatalytic activity of transition metal oxides?, ACS Catalysis, 5 (2015) 869-873.

[15] W.T. Hong, K.A. Stoerzinger, Y.-L. Lee, L. Giordano, A. Grimaud, A.M. Johnson, J. Hwang, E.J. Crumlin, W. Yang, Y. Shao-Horn, Charge-transfer-energy-dependent oxygen evolution reaction mechanisms for perovskite oxides, Energy & Environmental Science, 10 (2017) 2190-2200.

[16] J. Zhang, W. Li, J. Wang, X. Pu, G. Zhang, S. Wang, N. Wang, X. Li, Engineering p‐Band Center of Oxygen Boosting H+ Intercalation in δ‐MnO2 for Aqueous Zinc Ion Batteries, Angewandte Chemie International Edition, 62 (2023) e202215654.

[17] J.H. Park, C.H. Lee, J.-M. Ju, J.-H. Lee, J. Seol, S.U. Lee, J.-H. Kim, Bifunctional Covalent Organic Framework-Derived Electrocatalysts with Modulated p-Band Centers for Rechargeable Zn–Air Batteries, Advanced Functional Materials, 31 (2021) 2101727.

[18] Z. Liu, Y. Sun, X. Wu, C. Hou, Z. Geng, J. Wu, K. Huang, L. Gao, S. Feng, Charge transfer-induced O p-band center shift for an enhanced OER performance in LaCoO 3 film, CrystEngComm, 21 (2019) 1534-1538.

[19] S.-H. Wei, L. Ferreira, J.E. Bernard, A. Zunger, Electronic properties of random alloys: Special quasirandom structures, Physical Review B, 42 (1990) 9622.

[20] D. Ding, X. Li, S.Y. Lai, K. Gerdes, M. Liu, Enhancing SOFC cathode performance by surface modification through infiltration, Energy & Environmental Science, 7 (2014) 552-575.

[21] S. Chen, H. Zhang, C. Yao, H. Lou, M. Chen, X. Lang, K. Cai, Review of SOFC cathode performance enhancement by surface modifications: Recent advances and future directions, Energy & Fuels, 37 (2023) 3470-3487.

[22] C. Ling, R. Zhang, H. Jia, Quantum chemical design of doped Ca2MnAlO5+δ as oxygen storage media, ACS Applied Materials & Interfaces, 7 (2015) 14518-14527.

[23] Z. Shao, S.M. Haile, A high-performance cathode for the next generation of solid-oxide fuel cells, Nature, 431 (2004) 170-173.

[24] H.A. Tahini, X. Tan, W. Zhou, Z. Zhu, U. Schwingenschlögl, S.C. Smith, Sc and Nb dopants in $SrCoO_3$ modulate electronic and vacancy structures for improved water splitting and SOFC cathodes, Energy Storage Materials, 9 (2017) 229-234.

[25] J.W. Han, B. Yildiz, Mechanism for enhanced oxygen reduction kinetics at the (La, Sr)$CoO_{3-\delta}$/(La, Sr)$_2CoO_{4+\delta}$ hetero-interface, Energy & Environmental Science, 5 (2012) 8598-8607.

[26] X. Li, H. Zhao, J. Liang, Y. Luo, G. Chen, X. Shi, S. Lu, S. Gao, J. Hu, Q. Liu, A-site perovskite oxides: an emerging functional material for electrocatalysis and photocatalysis, Journal of materials chemistry A, 9 (2021) 6650-6670.

[27] Z. Feng, E.J. Crumlin, W.T. Hong, D. Lee, E. Mutoro, M.D. Biegalski, H. Zhou, H. Bluhm, H.M. Christen, Y. Shao-Horn, In situ studies of the temperature-dependent surface structure and chemistry of single-crystalline (001)-oriented $La_{0.8}Sr_{0.2}CoO_{3-\delta}$ perovskite thin films, The Journal of Physical Chemistry Letters, 4 (2013) 1512-1518.

[28] B. Koo, K. Kim, J.K. Kim, H. Kwon, J.W. Han, W. Jung, Sr segregation in perovskite oxides: why it happens and how it exists, Joule, 2 (2018) 1476-1499.

[29] R. Jacobs, J. Liu, B.T. Na, B. Guan, T. Yang, S. Lee, G. Hackett, T. Kalapos, H. Abernathy, D. Morgan, Unconventional Highly Active and Stable Oxygen Reduction Catalysts Informed by Computational Design Strategies, Advanced Energy Materials, 12 (2022) 2201203.

[30] S. Akrami, P. Edalati, M. Fuji, K. Edalati, High-entropy ceramics: Review of principles, production and applications, Materials Science and Engineering: R: Reports, 146 (2021) 100644.

[31] F. He, F. Zhu, D. Liu, Y. Zhou, K. Sasaki, Y. Choi, M. Liu, Y. Chen, A reversible perovskite air electrode for active and durable oxygen reduction and evolution reactions via the A-site entropy engineering, Materials Today, (2023).

[32] R. Witte, A. Sarkar, R. Kruk, B. Eggert, R.A. Brand, H. Wende, H. Hahn, High-entropy oxides: An emerging prospect for magnetic rare-earth transition metal perovskites, Physical Review Materials, 3 (2019) 034406.

[33] K. Xu, F. Zhu, M. Hou, C. Li, H. Zhang, Y. Chen, Activating and stabilizing the surface of anode for high-performing direct-ammonia solid oxide fuel cells, Nano Research, 16 (2023) 2454-2462.

[34] Y. Pan, K. Pei, Y. Zhou, T. Liu, M. Liu, Y. Chen, A straight, open and macro-porous fuel electrode-supported protonic ceramic electrochemical cell, Journal of Materials Chemistry A, 9 (2021) 10789-10795.

[35] F. Dong, D. Chen, Y. Chen, Q. Zhao, Z. Shao, La-doped BaFeO 3− δ perovskite as a cobalt-free oxygen reduction electrode for solid oxide fuel cells with oxygen-ion conducting electrolyte, Journal of Materials Chemistry, 22 (2012) 15071-15079.

[36] F. Dong, M. Ni, W. He, Y. Chen, G. Yang, D. Chen, Z. Shao, An efficient electrocatalyst as cathode material for solid oxide fuel cells: BaFe0· 95Sn0· 05O3− δ, Journal of Power Sources, 326 (2016) 459-465.

[37] G. Kresse, J. Hafner, Ab initio molecular dynamics for liquid metals, Physical Review B, 47 (1993) 558-561.

[38] G. Kresse, J. Furthmuller, Efficient iterative schemes for ab initio total-energy calculations using a plane-wave basis set, Physical Review B, 54 (1996) 11169-11186.

[39] P.E. Blöchl, Projector augmented-wave method, Physical Review B, 50 (1994) 17953-17979.

[40] J.P. Perdew, K. Burke, M. Ernzerhof, Generalized Gradient Approximation Made Simple, Physical Review Letters, 77 (1996) 3865-3868.

[41] S.L. Dudarev, G.A. Botton, S.Y. Savrasov, C.J. Humphreys, A.P. Sutton, Electron-energy-loss spectra and the structural stability of nickel oxide: An LSDA+U study, Physical Review B, 57 (1998) 1505-1509.

[42] A.M. Ritzmann, J.M. Dieterich, E.A. Carter, Density functional theory + U analysis of the electronic structure and defect chemistry of LSCF ($La_{0.5}Sr_{0.5}Co_{0.25}Fe_{0.7}5O_{3-\delta}$), Physical Chemistry Chemical Physics, 18 (2016) 12260-12269.

[43] J. Zan, S. Wang, D. Zheng, F. Li, W. Chen, Q. Pei, L. Jiang, Characterization and functional application of $PrBa_{0.5}Sr_{0.5}Co_{1.5}Fe_{0.5}O_{5+\delta}$ cathode material for IT-SOFC, Materials Research Bulletin, 137 (2021) 111173.

[44] L. Shen, Z. Du, Y. Zhang, X. Dong, H. Zhao, Medium-entropy perovskites Sr ($Fe_{\alpha}Ti_{\beta}Co_{\gamma}Mn_{\zeta}$)$O_{3-\delta}$ as promising cathodes for intermediate temperature solid oxide fuel cell, Applied Catalysis B: Environmental, 295 (2021) 120264.

[45] B. Zhang, Y. Wan, Z. Hua, K. Tang, C. Xia, Tungsten-doped $PrBaFe_2O_{5+\delta}$ double perovskite as a high-performance electrode material for symmetrical solid oxide fuel cells, ACS Applied Energy Materials, 4 (2021) 8401-8409.

[46] Y. Li, J. Cai, J.A. Alonso, H. Lian, X. Cui, J.B. Goodenough, Evaluation of $LaNi_{0.\,6}M_{0.\,4}O_3$ (M= Fe, Co) cathodes in LSGM-electrolyte-supported solid-oxide fuel cells, International Journal of Hydrogen Energy, 42 (2017) 27334-27342.

[47] Z. Yang, C. Yang, C. Jin, M. Han, F. Chen, $Ba_{0.9}Co_{0.7}Fe_{0.2}Nb_{0.1}O_{3-\delta}$ as cathode material for intermediate temperature solid oxide fuel cells, Electrochemistry Communications, 13 (2011) 882-885.

[48] F. Zhu, F. He, K. Xu, Y. Chen, Enhancing the oxygen reduction reaction activity and durability of a double-perovskite via an A-site tuning, Science China Materials, 65 (2022) 3043-3052.

[49] L. Fan, Y. Wang, Z. Jia, Y. Xiong, M.E. Brito, Nanofiber-structured SSC–GDC composite cathodes for a LSGM electrolyte based IT-SOFCs, Ceramics International, 41 (2015) 6583-6588.

[50] Z. Du, K. Li, H. Zhao, X. Dong, Y. Zhang, K. Świerczek, A $SmBaCo_2O_{5+\delta}$ double perovskite with epitaxially grown $Sm_{0.2}Ce_{0.8}O_{2-\delta}$ nanoparticles as a promising cathode for solid oxide fuel cells, Journal of Materials Chemistry A, 8 (2020) 14162-14170.

[51] F. He, F. Zhu, D. Liu, Y. Zhou, K. Sasaki, Y. Choi, M. Liu, Y. Chen, A reversible perovskite air electrode for active and durable oxygen reduction and evolution reactions via the A-site entropy engineering, Materials Today, 63 (2023) 89-98.

[52] L. Zhang, M. Liu, J. Huang, Z. Song, Y. Fu, Y. Chang, C. Li, T. He, Improved thermal expansion and electrochemical performances of Ba0. 6Sr0. 4Co0. 9Nb0. 1O3− δ–Gd0. 1Ce0. 9O1. 95 composite cathodes for IT-SOFCs, international journal of hydrogen energy, 39 (2014) 7972-7979.

[53] A. Grimaud, F. Mauvy, J.M. Bassat, S. Fourcade, M. Marrony, J.C. Grenier, Hydration and transport properties of the $Pr_{2-x}Sr_xNiO_{4+\delta}$ compounds as H^+-SOFC cathodes, Journal of Materials Chemistry, 22 (2012) 16017-16025.

[54] Y. Takeda, R. Kanno, M. Noda, Y. Tomida, O. Yamamoto, Cathodic polarization phenomena of perovskite oxide electrodes with stabilized zirconia, Journal of the Electrochemical Society, 134 (1987) 2656.

[55] A.V. Krukau, O.A. Vydrov, A.F. Izmaylov, G.E. Scuseria, Influence of the exchange screening parameter on the performance of screened hybrid functionals, Journal of Chemical Physics, 125 (2006) 224106.

[56] R. Jacobs, J. Hwang, Y. Shao-Horn, D. Morgan, Assessing Correlations of Perovskite Catalytic Performance with Electronic Structure Descriptors, Chemistry of Materials, 31 (2019) 785-797.

[57] R. Jacobs, T. Mayeshiba, J. Booske, D. Morgan, Material Discovery and Design Principles for Stable, High Activity Perovskite Cathodes for Solid Oxide Fuel Cells, Advanced Energy Materials, 8 (2018) 1702708.

[58] Y. Choi, M.C. Lin, M. Liu, Rational design of novel cathode materials in solid oxide fuel cells using first-principles simulations, Journal of Power Sources, 195 (2010) 1441-1445.

[59] Z.W. Seh, J. Kibsgaard, C.F. Dickens, I. Chorkendorff, J.K. Nørskov, T.F. Jaramillo, Combining theory and experiment in electrocatalysis: Insights into materials design, Science, 355 (2017) eaad4998.

[60] S. Lee, M. Kim, K.T. Lee, J.T. Irvine, T.H. Shin, Enhancing electrochemical CO2 reduction using Ce (Mn, Fe) O2 with La (Sr) Cr (Mn) O3 cathode for high‐temperature solid oxide electrolysis cells, Advanced Energy Materials, 11 (2021) 2100339.

[61] P. Caliandro, A. Nakajo, S. Diethelm, Model-assisted identification of solid oxide cell elementary processes by electrochemical impedance spectroscopy measurements, Journal of Power Sources, 436 (2019) 226838.

[62] F. He, M. Hou, F. Zhu, D. Liu, H. Zhang, F. Yu, Y. Zhou, Y. Ding, M. Liu, Y. Chen, Building efficient and durable hetero-interfaces on a perovskite‐based electrode for electrochemical CO_2 reduction, Advanced Energy Materials, (2022) 2202175.

[63] S. Lee, M. Kim, K.T. Lee, J.T. Irvine, T.H. Shin, Enhancing electrochemical CO_2 reduction using $Ce(Mn, Fe)O_2$ with $La(Sr)Cr(Mn)O_3$ cathode for high‐temperature solid oxide electrolysis cells, Advanced Energy Materials, 11 (2021) 2100339.

[64] Y. Gou, G. Li, R. Ren, C. Xu, J. Qiao, W. Sun, K. Sun, Z. Wang, Pr-doping motivating the phase transformation of the $BaFeO_{3-\delta}$ perovskite as a high-performance solid oxide fuel cell cathode, ACS Applied Materials & Interfaces, 13 (2021) 20174-20184.

[65] D. Panthi, A. Tsutsumi, Micro-tubular solid oxide fuel cell based on a porous yttria-stabilized zirconia support, Scientific reports, 4 (2014) 1-6.

[66] S.-L. Zhang, H. Wang, T. Yang, M.Y. Lu, C.-X. Li, C.-J. Li, S.A. Barnett, Advanced oxygen-electrode-supported solid oxide electrochemical cells with $Sr(Ti, Fe)O_{3-\delta}$-based fuel electrodes for electricity generation and hydrogen production, Journal of Materials Chemistry A, 8 (2020) 25867-25879.

[67] Q. Yang, G. Wang, H. Wu, B.A. Beshiwork, D. Tian, S. Zhu, Y. Yang, X. Lu, Y. Ding, Y. Ling, A high-entropy perovskite cathode for solid oxide fuel cells, Journal of Alloys and Compounds, 872 (2021) 159633.

[68] H. Wang, W. Ji, L. Zhang, Y. Gong, B. Xie, Y. Jiang, Y. Song, Preparation of YSZ films by magnetron sputtering for anode-supported SOFC, Solid State Ionics, 192 (2011) 413-418.

[69] T. Guo, X. Dong, M.M. Shirolkar, X. Song, M. Wang, L. Zhang, M. Li, H. Wang, Effects of cobalt addition on the catalytic activity of the Ni-YSZ anode functional layer and the

electrochemical performance of solid oxide fuel cells, ACS Applied Materials & Interfaces, 6 (2014) 16131-16139.

[70] B. Liu, X. Chen, Y. Dong, S.S. Mao, M. Cheng, A High‐performance, nanostructured $Ba_{0.5}Sr0.5Co_{0.8}Fe_{0.2}O_{3-\delta}$ cathode for solid‐oxide fuel cells, Advanced Energy Materials, 1 (2011) 343-346.

[71] H. Yang, Y. Gu, Y. Zhang, Y. Zheng, Z. Zhang, L. Ge, H. Chen, L. Guo, Sr-substituted $SmBa_{0.75}Ca_{0.25}CoFeO_{5+\delta}$ as a cathode for intermediate-temperature solid oxide fuel cells, Journal of Alloys and Compounds, 770 (2019) 616-624.

[72] M. López-Robledo, M. Laguna-Bercero, A. Larrea, V. Orera, Reversible operation of microtubular solid oxide cells using $La_{0.6}Sr_{0.4}Co_{0.2}Fe_{0.8}O_{3-\delta}$-$Ce_{0.9}Gd_{0.1}O_{2-\delta}$ oxygen electrodes, Journal of Power Sources, 378 (2018) 184-189.

[73] Y. Zhang, L. Shen, Y. Wang, Z. Du, B. Zhang, F. Ciucci, H. Zhao, Enhanced oxygen reduction kinetics of IT-SOFC cathode with $PrBaCo_2O_{5+\delta}/Gd_{0.1}Ce_{1.9}O_{2-\delta}$ coherent interface, Journal of Materials Chemistry A, 10 (2022) 3495-3505.

[74] Q. Yang, T. Sun, Y. Ding, X. Lu, D. Tian, B. Lin, Monovalent ion doping to enhance the performance of cobalt-free Sm0. 5Sr0. 5FeO3-δ cathode for YSZ fuel cells, Journal of Alloys and Compounds, 968 (2023) 171967.

[75] X. Li, C. Shi, G. Zhang, G. Zheng, Z. Huang, X. Shen, J. Zhou, T. Chen, S. Wang, A medium-entropy perovskite oxide La0. 7Sr0. 3Co0. 25Fe0. 25Ni0. 25Mn0. 25O3-δ as intermediate temperature solid oxide fuel cells cathode material, Ceramics International, 49 (2023) 30187-30195.

[76] Z. Wang, C. Yang, J. Pu, Y. Tian, J. Wang, F. Ciucci, B. Chi, In-situ self-assembly nano-fibrous perovskite cathode excluding Sr and Co with superior performance for intermediate-temperature solid oxide fuel cells, Journal of Alloys and Compounds, 947 (2023) 169470.

[77] Q. Yang, H. Ma, Y. Ding, X. Lu, Y. Chen, D. Tian, B. Lin, Na+ doping activates and stabilizes layered perovskite cathodes for high-performance fuel cells, Ceramics International, 49 (2023) 15599-15608.

[78] J.-H. Song, M.G. Jung, H.W. Park, H.-T. Lim, The effect of fabrication conditions for GDC buffer layer on electrochemical performance of solid oxide fuel cells, Nano-Micro Letters, 5 (2013) 151-158.

[79] P.J. Rivero, J. Goicoechea, A. Urrutia, F.J. Arregui, Effect of both protective and reducing agents in the synthesis of multicolor silver nanoparticles, Nanoscale research letters, 8 (2013) 1-9.

[80] K. Pei, Y. Zhou, Y. Ding, K. Xu, H. Zhang, W. Yuan, K. Sasaki, Y. Choi, M. Liu, Y. Chen, An improved oxygen reduction reaction activity and CO_2-tolerance of $La_{0.6}Sr_{0.4}Co_{0.2}Fe_{0.8}O_{3-\delta}$ achieved by a surface modification with barium cobaltite coatings, Journal of Power Sources, 514 (2021) 230573.

[81] Y. Chen, S. Yoo, Y. Choi, J.H. Kim, Y. Ding, K. Pei, R. Murphy, Y. Zhang, B. Zhao, W. Zhang, H. Chen, Y. Chen, W. Yuan, C. Yang, M. Liu, A highly active, CO_2-tolerant electrode for the oxygen reduction reaction, Energy & Environmental Science, 11 (2018) 2458-2466.

[82] M. Su, D. Huan, X. Hu, K. Zhu, R. Peng, C. Xia, Understanding the favorable CO_2 tolerance of Ca-doped $LaFeO_3$ perovskite cathode for solid oxide fuel cells, Journal of Power Sources, 521 (2022) 230907.